Boron, carbon, oxygen and radiogenic isotope investigation of carbonatite from the Miaoya complex, central China: Evidences for late-stage REE hydrothermal event and mantle source heterogeneity

Çimen O. [a,b,*], Kuebler C. [a], Monaco B. [a], Simonetti S.S. [a], Corcoran L. [a], Chen W. [c], Simonetti A. [a]

[a] University of Notre Dame, Department of Civil and Environmental Engineering and Earth Sciences, South Bend, IN 46556, USA
[b] Munzur University, Department of Geological Engineering, 62000 Tunceli, Turkey
[c] State Key Laboratory of Geological Processes and Mineral Resources, Collaborative Innovation Center for Exploration of Strategic Mineral Resources, China University of Geosciences, Wuhan 430074, China

ABSTRACT

The Miaoya carbonatite complex (MCC) is located within the southern edge of the Qinling orogenic belt in central China, and is associated with significant rare earth element (REE) and Nb mineralization. The MCC consists of syenite and carbonatite that were emplaced within Neo- to Mesoproterozoic-aged supracrustal units. The carbonatite intruded the associated syenite as stocks and dikes, and is mainly composed of medium- to fine-grained calcite and abundant REE-bearing minerals. Carbonatite melt generation and emplacement within the MCC occurred during the Silurian (at ~440 Ma), and was subsequently impacted by a late-stage hydrothermal event (~232 Ma) involving REE-rich fluids/melt.

This study reports trace element and stable (B, C, and O) and radiogenic (Nd, Pb, and Sr) isotope data for the MCC carbonatite, and these have been subdivided into three groups that represent different REE contents, interpreted as varying degrees of hydrothermal interaction. Overall, the group of carbonatites with the lowest enrichment in LREEs (i.e., least affected by hydrothermal event) is characterized by $\delta^{11}B$ values that vary between -7 (typical asthenospheric mantle) and $+ 4‰$; $\delta^{11}B$ values and B abundances (~0.2 to ~1 ppm) do not correlate with LREE contents. The Sm-Nd and Pb-Pb isotope systems have both been perturbed by the late-stage, REE-rich hydrothermal activity and corroborate open-system behavior. Contrarily, initial $^{87}Sr/^{86}Sr$ ratios (vary between ~0.70355 and 0.70385) do not correlate significantly with both LREEs and Sr abundances, nor with initial $^{143}Nd/^{144}Nd$ ratios. The late-stage hydrothermal event overprinted the Nd and Pb isotope compositions for most of the carbonatite samples examined here, whereas a majority of the samples preserve their variable B and Sr isotope values inherited from their mantle source. The B and Sr isotope data for carbonatites exhibiting the least LREE enrichment correlate positively and suggest carbonatite melt generation from a heterogenous upper mantle source that records the input of recycled crustal material. This finding is consistent with those previously reported for young (<300 Ma old) carbonatites worldwide.

© 2018 Elsevier B.V. All rights reserved.

1. Introduction

Carbonatites are igneous rocks that consist of >50% carbonate minerals and contain high concentrations of incompatible elements, such as Sr, Ba, P and light rare earth elements (LREEs; e.g., Nelson et al., 1988; Jones et al., 2013). Their unique chemical composition combined with their low viscosity (e.g., Treiman and Schedl, 1983) enables them to rapidly ascend through the subcontinental lithospheric mantle (SCLM) and overlying crust, with the increased likelihood of preserving the isotopic signatures inherited from their mantle source region. Carbonatites are generally found within stable, intra-plate, continental regions and continental rifts, and rarely in orogenic belts or within oceanic plates (Woolley, 1989; Woolley and Kjarsgaard, 2008). The exact origin of carbonatitic melts remains a matter of debate and there are three main mechanisms that have been proposed for their genesis: 1- derivation by direct partial melting of a mantle source (e.g., Dasgupta and Walker, 2008; Gittins and Harmer, 2003; Russell et al., 2012), 2- product of liquid immisibilty from carbonated silicate rocks (e.g., Fischer et al., 2009; Lee et al., 2000; Lee and Wyllie, 1998) such as allikites (e.g., Tappe et al., 2005), or 3- extreme melt differentiation resulting from prolonged fractional crystallization of a parental carbonated silicate magma (e.g., Cooper et al., 2011; Mitchell, 2005; Veksler et al., 1998).

The mantle sources giving rise to carbonatite melts and nature of mantle carbon (C) contained within carbonatites are also both

* Corresponding author.
  E-mail address: ocimen@nd.edu (O. Çimen).

contentious issues (see Bell and Simonetti, 2010 for detailed review). In general, there are two main hypotheses, one advocates for carbonatite melts being derived solely within the subcontinental lithospheric mantle (SCLM; e.g., Bailey, 1993a). The main argument for sole lithospheric involvement is the repeated occurrence of carbonatite magma emplacement in the same location within continents over billions of years (e.g., Greenland; Larsen and Rex, 1992). Moreover, Bailey (1993a, 1993b) argues that the repeated alkaline magmatic activity in East Africa is the result of localization of carbonatite melts by old lesions in the lithosphere. The second hypothesis advocates for an asthenospheric origin for the source of mantle C, which is based primarily on the results from numerous, previous radiogenic (Nd, Pb, Sr), stable (C, O) and noble gas (Xe, Kr, Ne) isotopic studies of carbonatites and associated alkaline silicate rocks (as summarized in Bell and Simonetti, 2010). In brief, the radiogenic isotope systematics of young carbonatite complexes (<200 Ma old) worldwide indicate that these are derived from a heterogeneous (mixed) mantle source consisting predominantly of EMI (Enriched Mantle I) and HIMU (high-μ; $^{238}U/^{204}Pb$) mantle components (Zindler and Hart, 1986). The latter feature is consistent with the radiogenic isotope characteristics of oceanic island basalts (OIBs), and therefore, carbonatite magma genesis has been linked to mantle plume activity (e.g., Bell and Simonetti, 1996; Bell and Simonetti, 2010; Simonetti et al., 1995; Simonetti et al., 1998). In the mantle plume-related hypothesis, carbonatite melts represent magmas derived from a volatile-rich, asthenospheric/plume source that are trapped by the overlying lithosphere, which is then subjected to repeated episodes of metasomatism (Bell and Simonetti, 2010).

The source of mantle C within carbonatitic melts may be either juvenile (primordial) or recycled in nature, or a combination of both (e.g., Bell and Simonetti, 2010; Hulett et al., 2016). The incorporation of C from various mantle sources, whether recycled in nature, lithospheric or asthenospheric, into carbonate liquids is probably the result of a complicated process, and dependent on the stability of carbonate minerals and mantle oxidation state (e.g., Luth, 1993). Recently, on the basis of their heavier ($\delta^{11}B > -7‰$) boron isotopic signatures, Hulett et al. (2016) argued that carbonatite occurrences worldwide <300 million years old record the presence of subducted, crustal carbon. Contrarily, most of the older carbonatite complexes are characterized by much lower $\delta^{11}B$ values (~ $-7‰$), overlapping that of asthenospheric mantle (~ $-7 \pm 1‰$; Chaussidon and Jambon, 1994). The change (increase) to more positive boron isotope values with decreasing geologic time was attributed to fundamental change in Earth's geodynamics and tectonism, with progressive establishment of modern-style plate tectonics and increased plume activity (Hulett et al., 2016). Bell and Tilton (2001) proposed that subducted lithosphere may sink to the core-mantle boundary (D"layer), and subsequent a long period of storage (billions of years?), recycled lithospheric (crustal) components may be transported to shallower depths by ascending mantle plumes, which may be tapped during carbonatite melt generation.

To date, the majority of previous investigations have focused on carbonatites within anorogenic tectonic environments, whereas collision/subduction zone-related carbonatite complexes have received less attention (e.g., Hou et al., 2006). Several previous studies that investigated carbonatite complexes associated with subduction/collision zones have suggested these are derived from the overriding, metasomatised lithospheric mantle wedge (e.g., Bonadiman et al., 2008; Deng et al., 2014; D'Orazio et al., 2007). In this hypothesis, carbonatite melts may form by melting of metasomatized SCLM that was modified by infiltration of high-flux REE- and CO_2-rich fluids derived from subducted marine sediments (e.g., Hou et al., 2006, 2015).

To this end, this study focuses on the geochemical and isotopic investigation of the Miaoya carbonatite complex (MCC), which is located within a major collision/tectonic zone in central China, and has been identified as an important economic source of rare earth element (REE) mineralization (e.g., Xu et al., 2010). Unlike other REE deposits within China, Xu et al. (2010) noted the lack of evidence for hydrothermal mineralization present within the MCC. Xu et al. (2010) advocated that the MCC carbonatites formed via multi-stage fractional crystallization from an initial REE-rich carbonatitic liquid. Subsequently, Xu et al. (2014, 2015) proposed a more complex model for the generation of the MCC that involved recycling of the Mianlue oceanic crust (Triassic), and a REE-rich carbonate liquid derived from an ancient, deep-seated mantle source (generated from Proterozoic recycled carbonates or carbonated peridotite). Recently, Zhu et al. (2017) suggested that the MCC formed in an extensional rift setting, associated with mantle upwelling.

Based on numerous previous studies, the emplacement age of the MCC is somewhat controversial since widely discrepant dates have been reported (Ying et al., 2017). For example, ages between 233 and 434 Ma and 147 and 766 Ma have been reported for the carbonatite and associated syenite, respectively (Xu et al., 2014, 2015; Zhu et al., 2017). However, a recent, detailed geochronological investigation (Ying et al., 2017) reports in-situ U-Pb dating results for several minerals (i.e., zircon, monazite and columbite) from the MCC in order to better understand its emplacement age and formational history. According to the results from Ying et al. (2017), there were two major episodes of activity associated with the MCC, one magmatic event that occurred between 426 and 442 Ma, and a second, metasomatic event at 232 Ma.

This study reports new and combined geochemical data, radiogenic (Sr, Nd, Pb), stable (O and C), and for the first time boron isotope data for carbonate separates from MCC carbonatites in order to better evaluate their petrogenetic evolution; in particular, to better assess/delineate possible evidence(s) for late-stage hydrothermal activity, and consequently provide useful insights relative to the chemical nature of the mantle source.

2. Geological setting

Central China consists of the North China Block and South China Block, separated by the Qinling orogenic belt (Fig. 1a). The MCC is located in the southern edge of the Qinling belt which, in-turn, is divided into northern and southern sections by the Shangdan suture (Fig. 1b). The Qinling Precambrian basement consists of late Archean to Paleoprotorezoic crystalline rocks and Meso- to Neoproterozoic supracrustal units (Xu et al., 2008 and references therein). The crystalline basement (Qinling and Douling groups) includes mostly granulite and amphibolite facies products, whereas the supracrustal sections (Kuanping, Wudang and Yaolinghe groups) contain low-grade metamorphic units (Xu et al., 2008). This region has experienced several tectonic events that include development of early-to-mid Proterozoic rifting, subduction/collision-related events until the Early Mesozoic, and orogenic processes that occurred post-Mesozoic (Ying et al., 2017 and references therein). Silurian rifting in the region (opening of the Mianlue Ocean) resulted in the generation of ultramafic to mafic dyke swarms, alkali lamprophyre, carbonatite and syenite (Ying et al., 2017). The late Permian-Triassic collision between the North China Block and South China Block is attributed to the closure of the Mialue ocean and formed one of the largest, ultra-high-pressure metamorphic zones on Earth, the Dabie-Sulu orogenic belt (Ying et al., 2017 and references therein). The North Qinling is characterized by widespread Paleozoic island-arc magmatism and metamorphism, whereas the South Qinling is defined by the occurrence of Triassic syn-collision granitic magmatism and ultra-high pressure metamorphism (Xu et al., 2010 and references therein).
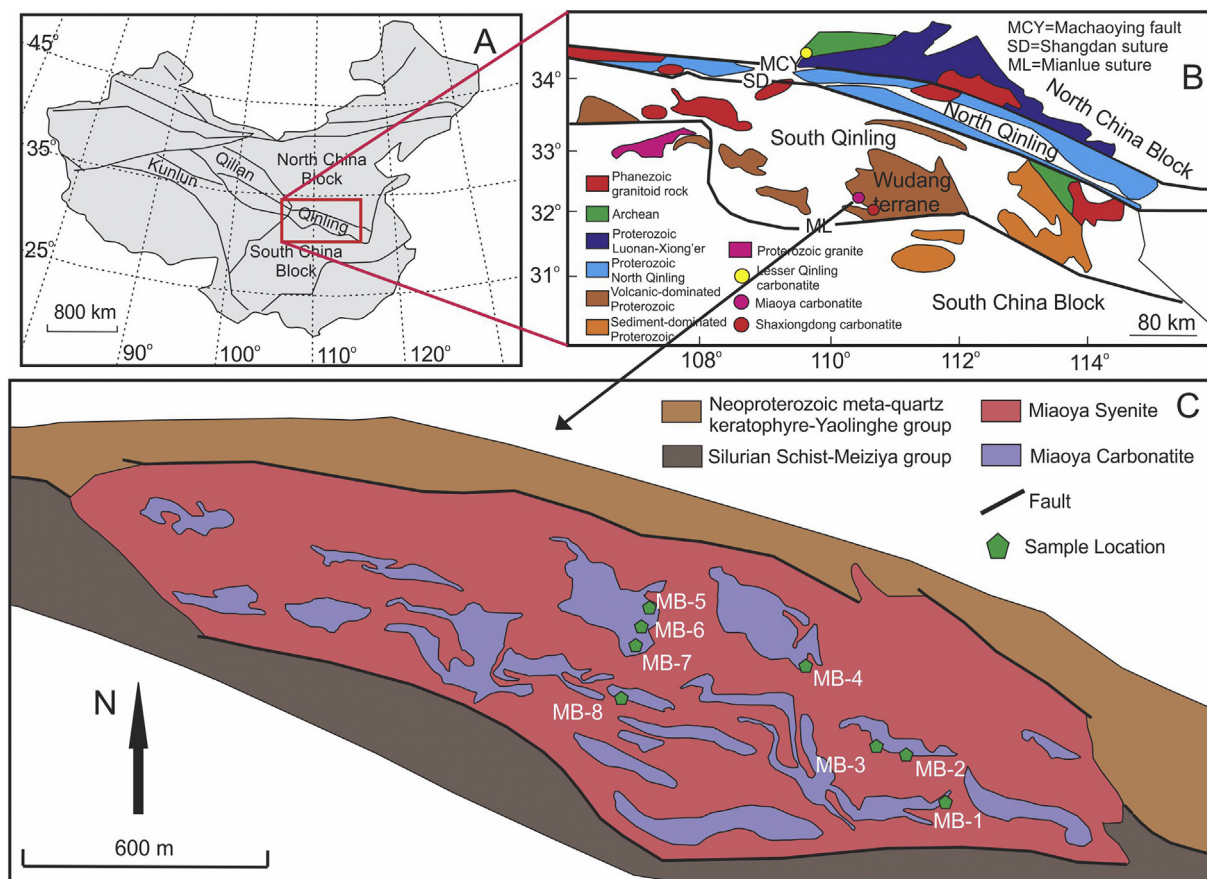
Fig. 1. Regional map of China (A), and location (B) and geological (C) maps of the Miaoya carbonatite complex (modified from Xu et al., 2015; Ying et al., 2017; Chen et al., 2018).

The MCC is located in the southwestern margin of the Wudang terrane (Fig. 1b), which includes alkaline basalt, keratophyre, quartz-keratophyre, dacite rhyolite and pyroclastic rocks. The Yaolinghe metamorphic rocks, a part of the Wudang terrane, are composed of tholeiite, spilitic diabase, spilite, keratophyre and interbedded clastics (Huang, 1993; Xu et al., 2014; Ying et al., 2017). Two members of the Yaolinghe metamorphic terrane, the Yaolinghe metaquartz keratophyre and Meiziya schist, are cut by the MCC in a NW/W-SE/E direction (Fig. 1c; Ling et al., 2008; Ying et al., 2017). The carbonatite intruded the associated syenite as stocks and dikes, and is mostly composed of fine- to medium-grained calcite (between 50 and 600 μm in size; Fig. 2) and rare earth element (REE)-bearing minerals (e.g., apatite, bastnaesite, columbite, and monazite up to 5 vol%). The majority of calcite grains are predominantly fresh (non-altered), subhedral to euhedral, exhibit polysynthetic twinning and may exhibit a bimodal grain size distribution (Fig. 2j). The common accessory minerals are mica, apatite, feldspar, albite, chlorite, zircon, niobium rutile, columbite, bastnaesite, pyrite, and monazite (carbonatite mineralogy also described in Xu et al., 2010 and Ying et al., 2017; Fig. 2). In general, apatite crystals in the samples investigated here are predominantly subhedral and rarely prismatic and associated with calcite (Figs. 2a, c, e, f). Biotite displays brownish colors with subhedral to euhedral crystals and are marginally replaced by iron oxide minerals. Pyrite crystals are predominantly euhedral (cubic) in shape. Evidence of possible late-stage hydrothermal alteration can be observed along fractures and grain boundaries of calcite crystals (Fig. 2j). The economic potential

of the MCC is estimated to be ~1.21 Mt. REE$_2$O$_3$ at an average grade of 1.72% (Xu et al., 2010).

3. Analytical methods

3.1. μXRF mapping

Petrographic thin sections (~100 μm thick) of carbonatite samples investigated here were examined using optical microscopy, and qualitative chemical maps (Si, Al, Mg, K, Ti, Ca, Fe, P) were obtained with an Edax Orbis micro-XRF instrument at the Center for Environmental Science and Technology (CEST), University of Notre Dame. The X-ray conditions employed were as follows: amplifier time 12.8 μs, fluorescent energy 32 kV, beam size 30 μm.

3.2. Microprobe analyses

The major and minor element concentrations (Table 1) of carbonate grains were analysed by electron microprobe (EMP) using a CAMECA SX-50 at the University of Notre Dame. All thin sections (~100 μm) were carbon-coated prior to analysis. The EMP instrument was operated with 15 kV of accelerating voltage, 10 nA of beam current, and 15 μm of beam diameter. The following standards were analysed for calibration purposes: TAP for Mg, PETJ for Ca, Sr, Mn, and LIFT for Fe. The peak and background counting times were 30 s for Mn and Fe, 25 s for Sr, 15 s for Mg, and 5 s for Ca.
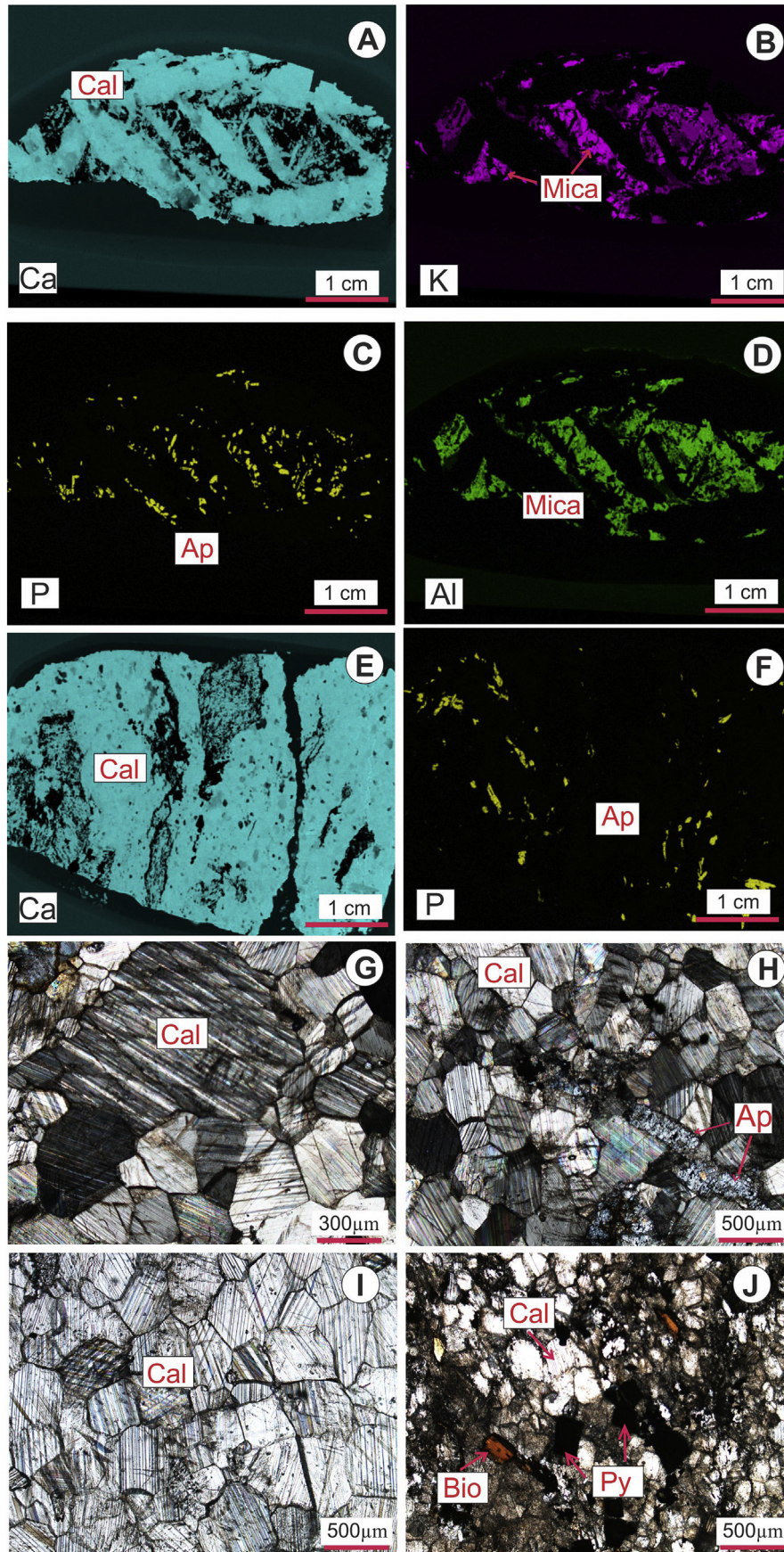
Fig. 2. Micro-XRF images illustrating distribution of Ca (A), K (B), P (C), and Al (D) for samples MB-1 (A to D) and MB-7 (E, F) showing presence of medium-to-fine-grained calcite (Cal), mica and apatite (Ap); Thin section images of samples MB-5 (G, H), MB-3A (I), and MB-8 (J) displaying the predominance of calcite with minor apatite, biotite (Bio), and pyrite (Py) grains.

Table 1
Major and minor element abundances (wt%) for five of the MCC carbonatite samples.

Sample/point	MgO	FeO	MnO	CaO	SrO	SUM
MB-1-1	0.20	0.46	0.23	51.05	2.36	54.30
MB-1-2	0.21	0.53	0.24	52.92	2.41	56.30
MB-1-3	0.27	0.76	0.29	50.62	2.29	54.24
MB-1-4	0.09	0.25	0.21	51.27	2.64	54.46
MB-1-5	0.11	0.33	0.27	51.58	2.57	54.85
MB-1-6	0.25	0.95	0.39	50.73	1.93	54.24
MB-1-7	0.35	1.59	0.37	50.20	1.50	54.01
MB-1-8	0.22	0.78	0.29	50.65	2.25	54.18
MB-1-9	0.12	0.30	0.25	51.71	2.45	54.82
MB-1-10	0.22	0.59	0.29	50.97	2.69	54.77
MB-1-11	0.12	0.31	0.31	51.13	2.67	54.53
MB-3A-1	0.45	1.46	0.55	51.00	1.72	55.16
MB-3A-2	0.43	1.32	0.52	50.97	1.59	54.82
MB-3A-3	0.43	1.40	0.51	51.00	1.58	54.92
MB-3A-4	0.41	1.37	0.55	51.19	1.67	55.18
MB-3A-5	0.42	1.38	0.50	50.86	1.73	54.88
MB-3A-6	0.40	1.39	0.54	50.80	1.54	54.66
MB-3A-7	0.37	1.29	0.52	51.03	1.38	54.59
MB-3A-8	0.40	1.32	0.50	51.34	1.41	54.95
MB-3A-9	0.39	1.25	0.50	51.06	1.40	54.60
MB-3A-10	0.40	1.34	0.53	51.33	1.42	55.03
MB-3B-1	0.49	1.73	0.54	51.29	1.43	55.48
MB-3B-2	0.66	2.06	0.55	50.81	1.49	55.56
MB-3B-3	0.75	2.18	0.56	50.27	1.36	55.13
MB-3B-4	0.76	2.23	0.55	50.23	1.39	55.16
MB-3B-5	0.90	2.57	0.62	49.56	1.26	54.90
MB-3B-6	0.97	2.64	0.61	49.12	1.24	54.58
MB-3B-7	0.84	2.49	0.56	49.87	1.26	55.01
MB-3B-8	0.59	2.07	0.55	50.40	1.09	54.69
MB-3B-9	0.52	1.95	0.53	50.53	1.45	54.97
MB-3B-10	0.53	2.00	0.56	50.69	1.54	55.32
MB-7-1	0.74	1.32	0.52	56.28	0.97	59.85
MB-7-2	0.21	0.39	0.25	52.72	1.28	54.86
MB-7-3	0.37	0.71	0.29	52.48	1.02	54.87
MB-7-4	0.81	1.21	0.46	51.40	0.82	54.70
MB-7-5	0.53	0.88	0.34	51.84	1.09	54.68
MB-7-6	1.36	1.71	0.56	50.42	0.84	54.88
MB-7-7	0.73	1.30	0.55	51.19	0.84	54.60
MB-7-8	0.83	1.28	0.54	51.09	0.75	54.49
MB-7-9	0.63	0.96	0.40	51.75	0.93	54.66
MB-7-10	0.58	0.89	0.33	52.04	0.91	54.74
MB-7-11	0.57	0.92	0.36	53.73	0.92	56.49
MB-8-1	0.65	2.32	1.02	50.46	0.56	55.01
MB-8-2	1.20	3.28	0.98	48.58	0.54	54.57
MB-8-3	1.16	3.19	1.13	48.20	0.54	54.23
MB-8-4	0.57	2.29	1.05	49.67	0.66	54.24
MB-8-5	0.72	2.44	1.04	50.16	0.53	54.89
MB-8-6	0.99	2.97	1.07	49.55	0.57	55.16
MB-8-7	0.79	2.47	1.02	50.02	0.55	54.85
MB-8-8	0.68	2.34	0.99	50.32	0.54	54.86
MB-8-9	0.92	2.74	0.97	49.73	0.61	54.96
MB-8-10	0.84	2.67	1.01	49.79	0.55	54.85

3.3. Trace element determinations

Abundances for trace elements (Table 2) were determined on hand-picked, separated primary carbonate grains/fragments using a binocular microscope and these were processed and prepared in a class 1000 clean room facility at the Midwest Isotope and Trace Element Research Analytical Center (MITERAC), University of Notre Dame. The main reason for examining solely the carbonate fraction of each sample studied here is to conduct a valid comparison of their B isotope ratios to published values from carbonatites worldwide (Hulett et al., 2016); the latter study investigated solely the carbonate fraction of carbonatite samples and not whole rocks so as to eliminate the possibility of mineral-calcite boron isotope fractionation effects. However, Hulett et al. (2016) clearly demonstrated that the carbonate fraction controlled the mass balance of boron in the samples investigated. Details for analytical procedures described below are included within the appendix.

3.4. Stable (B, C, O) and radiogenic (Sr, Pb, Nd) isotope analyses

The $\delta^{18}O$ and $\delta^{13}C$ isotope data (Table 3) for carbonate separates examined here were obtained at CEST (University of Notre Dame) using a Delta V Advantage isotope ratio mass spectrometer. The appendix contains the detailed analytical procedure. Procedures for boron isotope analyses (Table 3) of carbonate separates were adapted from Hulett et al. (2016) and details are included within the appendix. Tables 4 and 5 list the Sr, Pb and Nd isotope analyses reported in this study. The appendix contains a brief description for each of the ion exchange chromatographies and analysis routines for Sr, Pb and Nd.

4. Results

4.1. Major and trace element geochemistry

Major and minor element abundances for five of the MCC carbonatite samples investigated here are listed in Table 1 and shown in Fig. 3, and these were selected to represent each one of the 3 groupings based on their relative rare earth element (REE) concentrations (Fig. 4). The EMP analyses (Table 1) indicate that the carbonate is calcite and chemical compositions can be highly variable within each sample with the exception of sample MB-3A (Fig. 3). In addition, there are no clear chemical trends in Fig. 3 that can be attributed to calcite fractional crystallization involving solely one parental melt.

The trace element abundances for carbonate separates from the MCC carbonatites are reported in Table 2. Previous investigations have reported and examined the trace element signatures of the MCC carbonatite (e.g., Xu et al., 2010, 2014, 2015), and in general, the abundances listed in Table 2 overlap those from older studies. For example, Fig. 4a illustrates and compares the chondrite normalized REE abundances for samples investigated here to those from Xu et al. (2010), and the data exhibit similar patterns and completely overlap. The total REE abundances range from 304 to 1926 ppm for carbonate separates analysed here, and chondrite normalized patterns display negative slopes and are devoid of Eu anomalies (Fig. 4a). The chondrite-normalized REE patterns exhibit variable degrees of enrichment in LREEs (e.g., $La/Sm_{(CN)} = 1.57–16.07$) and have subsequently been subdivided into three groups (Fig. 4a).

Boron concentrations for the carbonate fractions examined here are listed in Table 2 and shown in Fig. 4b, and these are compared to their corresponding total abundances of LREEs. All boron concentrations are <1 ppm, except for MB-8 (1.03 ppm), which overlap those for fresh (unaltered) MORBs (e.g., Spivack and Edmond, 1987; Wunder et al., 2005), and boron abundances reported for a majority of carbonatites worldwide (Hulett et al., 2016). Moreover, B contents for the carbonate fractions do not correlate with their corresponding total abundances of LREEs (Fig. 4b).

4.2. Boron, carbon and oxygen isotope data

The new O and C stable isotope data obtained for carbonate grains from the MCC samples are listed in Table 3 and illustrated in Fig. 5. The $\delta^{18}O_{SMOW}$ and $\delta^{13}C_{PDB}$ (‰) values for carbonates vary between +9.41 and + 12.51‰ and − 6.60 to −3.32‰, respectively, and overlap those reported in Xu et al. (2014). The $\delta^{13}C$ values fall within the range attributed to "primary igneous carbonatite (PIC)" ($\delta^{13}C \sim −4$ to $−8$‰; Keller and Hoefs, 1995); in contrast, with the exception of two samples (MB-3A, -3B) the remaining samples are characterized by heavier $\delta^{18}O$ values and plot to the right of the PIC box (Fig. 5). The latter overlap the field for C and O isotope values of carbonatites worldwide, and can be attributed to either Rayleigh crystal fractionation, or low temperature alteration, in particular if the $\delta^{18}O_{SMOW}$ values are > +14‰ (e.g., Deines, 1989).

Table 2
Trace element concentrations (ppm) for carbonate separates from the MCC carbonatites.

	MB-1	MB-2	MB-3A	MB-3B	MB-4A	MB-4B	MB-5	MB-6	MB-7	MB- 8
B	0.78	0.50	0.29	0.89	0.42	0.51	0.38	0.71	0.56	1.03
Cs	0.007	b.d.	0.005	0.001	0.003	0.001	0.007	0.010	0.010	0.016
Rb	0.077	0.004	0.099	0.054	0.118	0.033	0.078	0.120	0.046	0.096
Ba	169.5	51.3	81.4	465.4	73.4	119.7	466.6	52.0	297.3	75.1
W	0.156	0.009	0.039	b.d.	0.052	0.023	0.056	0.072	0.061	0.035
Th	0.649	1.825	0.145	0.053	0.522	0.196	0.230	0.703	0.385	0.377
U	4.00	0.07	0.95	0.20	0.45	0.16	1.23	1.52	0.45	0.53
Nb	1.15	0.54	0.19	0.27	9.11	5.83	10.41	1.65	1.35	1.22
Ta	0.002	b.d.	0.001	b.d.	0.024	0.010	0.041	0.015	0.003	0.011
La	379	337	37.1	63.3	253	169	107	25.4	252	41.8
Ce	376	361	50.6	38.5	337	158	112	47.8	90.0	55.0
Pb	2.53	2.39	2.44	2.23	10.72	5.85	2.56	3.03	2.91	4.66
Pr	34.76	36.18	6.14	5.03	32.78	16.47	13.76	6.59	10.16	7.44
Mo	1.17	1.09	0.62	1.15	0.52	0.46	0.16	1.05	1.11	0.39
Sr	9994	1236	6589	14,611	4946	4307	12,872	2102	14,984	3870
Nd	121	129	26.13	24.08	116.72	61.49	57.83	32.39	42.60	37.14
Sm	17.19	19.23	5.75	6.71	16.99	10.58	11.68	10.10	9.78	10.93
Zr	0.702	0.266	0.146	0.431	0.649	0.942	0.484	8.780	5.446	6.532
Hf	b.d.	b.d.	b.d.	b.d.	0.001	b.d.	0.002	0.049	0.004	0.024
Eu	5.05	5.66	2.15	2.79	4.95	3.39	3.90	4.25	3.40	4.14
Gd	13.56	15.00	6.69	8.82	13.14	8.95	10.67	12.31	10.08	12.98
Tb	1.67	1.93	1.01	1.46	1.65	1.21	1.50	1.92	1.43	1.91
Dy	8.86	9.97	6.54	8.99	8.64	6.67	8.36	11.23	8.16	10.45
Li	0.034	0.019	0.046	0.025	0.028	0.021	0.017	0.114	0.022	0.063
Y	76.7	75.2	67.3	189.7	55.2	66.0	98.6	73.3	234	92.9
Ho	1.59	1.74	1.40	1.74	1.59	1.24	1.56	2.07	1.59	1.89
Er	3.72	4.13	3.83	4.41	3.89	3.15	3.85	5.29	4.02	4.46
Tm	0.51	0.65	0.58	0.64	0.58	0.49	0.55	0.79	0.61	0.62
Yb	3.13	4.45	3.80	4.11	3.93	3.34	3.67	4.88	4.10	3.91
Lu	0.42	0.63	0.55	0.59	0.58	0.51	0.52	0.70	0.58	0.55
La/Sm(CN)	13.78	10.93	4.03	5.89	9.29	9.96	5.75	1.57	16.07	2.39
1/Sr	0.0001	0.0008	0.0002	0.0001	0.0002	0.0002	0.0001	0.0005	0.0001	0.0003
1/Nd	0.0083	0.0078	0.0383	0.0415	0.0086	0.0163	0.0173	0.0309	0.0235	0.0269

Note: b.d. = below detection limit, CN=Chondrite normalized.

The $\delta^{11}B$ (‰) isotope values for the carbonate separates from the same carbonatite samples range from −7.34‰ to +12.33‰ and are presented in Table 3 and shown in Fig. 6. Of note, there are four samples (MB-2, -3B, -4B, −7) that are characterized by negative $\delta^{11}B$ values, between −7.34‰ and − 5.56‰, which overlap the range attributed to typical asthenospheric (MORB) mantle of ~ −7 ± 1‰ (Chaussidon and Jambon, 1994). Hence, the PIC box outlined in Fig. 6 defines the combined B, C, and O isotope compositions of least differentiated carbonatite melts that may be derived from an asthenospheric mantle-like source. The remaining samples yield variable $\delta^{11}B$ compositions that range between −3.33‰ and 12.33‰ and are compared to their corresponding C and O isotope values (Fig. 6). The combined B, C, and O isotope data define different trends; for example, $\delta^{13}C$

values exhibit a restricted spread in values compared to $\delta^{11}B$ compositions (Fig. 6b), whereas $\delta^{18}O$ values plot along two different arrays with a common origin from the PIC box (Fig. 6a).

4.3. Sr, Nd, and Pb isotope compositions

The new Sr, Nd, and Pb isotope data for the MCC carbonate separates examined here are reported in Tables 4 and 5. Of note, the 232 Ma age reported by Ying et al. (2017) for the MCC carbonatites has been adopted for the age correction of all isotope ratios described below since the late-stage hydrothermal fluids/melts have impacted the isotope compositions. All of the carbonate samples are characterized by low $^{87}Rb/^{86}Sr$ values (0.00001 to 0.00017), resulting in minimal correction to the measured $^{87}Sr/^{86}Sr$ ratios that vary between 0.70357 and 0.70384 (Table 4). In contrast, the $^{147}Sm/^{144}Nd$ ratios vary between 0.085 and 0.188, which results in initial $^{143}Nd/^{144}Nd$ values that vary between 0.51220 and 0.51234 (Table 4). The initial ε_{Nd} values define a narrow range from +0.1 to −1.1, with the exception of one sample (MB-6), which has a slightly lower value of −2.7. The Sr and Nd isotope data reported here fall within the range of values previously obtained by Xu et al. (2014). A Sm-Nd isochron plot (not shown) that contains both data obtained here and those from previous investigations (Xu et al., 2014) both yield errorchrons that define young ages between ~100 and ~150 million years old and higher $^{147}Sm/^{144}Nd$ values compared to those from earlier studies (~800 ± ~500 million years old; Xu et al., 2014), respectively. Moreover, these younger Sm-Nd errorchron ages of between 100 and 150 Ma approach (given the associated uncertainty) the weighted mean $^{206}Pb/^{238}U$ age of 232.8 ± 4.5 Ma obtained for columbite (from carbonatite) and ~240 Ma old monazite (from carbonatite and syenite) by Ying et al. (2017) for the MCC carbonatites.

Table 3
C, O, and B isotope data for carbonate separates from the MCC carbonatites.

Sample	$\delta^{13}C$ (‰)	Uncertainty	$\delta^{18}O$ (‰)	Uncertainty	$\delta^{11}B$ (‰) [a]
MB-1	−6.24	0.03	12.13	0.03	2.55
MB-2	−3.32	0.02	12.51	0.05	−5.56
MB-3A	−6.00	0.03	9.41	0.03	−3.33
MB-3B	−5.93	0.03	9.85	0.06	−6.65
MB-4A	−4.40	0.05	11.88	0.04	12.33
MB-4B	−5.03	0.04	11.79	0.06	−6.26
MB-5	−6.60	0.03	10.08	0.04	1.41
MB-6	−4.25	0.03	10.78	0.04	2.82
MB-7	−4.89	0.05	10.80	0.08	−7.34
MB- 8	−4.59	0.03	12.14	0.04	3.89

[a] Uncertainty associated with B isotope ratios is ±0.5‰ (2 s level) based on replicate analyses of coral in-house standard (see text for details).

Table 4
Sr and Nd isotope data for carbonate separates from the MCC carbonatites.

Sample	Rb (ppm)	Sr (ppm)	$^{87}Rb/^{86}Sr$	$^{87}Sr/^{86}Sr$	2σ	$^{87}Sr/^{86}Sr$ (i)	Sm (ppm)	Nd (ppm)	$^{147}Sm/^{144}Nd$	$^{143}Nd/^{144}Nd$	2σ	$^{143}Nd/^{144}Nd$ (i)	εNd (t)
MB-1	0.15	19,920	0.00002	0.70383	0.00001	0.703829	17.2	121	0.085	0.51247	0.00001	0.51234	−0.1
MB-2	0.01	2465	0.00001	0.70376	0.00001	0.703763	19.2	129	0.090	0.51248	0.00001	0.51234	0.1
MB-3A	0.20	13,155	0.00004	0.70361	0.00001	0.703609	5.75	26.1	0.133	0.51251	0.00001	0.51230	−0.7
MB-3B	0.11	29,098	0.00001	0.70357	0.00002	0.703573	6.71	24.1	0.168	0.51254	0.00001	0.51228	−1.1
MB-4A	0.23	9808	0.00007	0.70361	0.00001	0.703614	17.0	117	0.088	0.51246	0.00001	0.51233	−0.2
MB-4B	0.06	8496	0.00002	0.70372	0.00002	0.703716	10.6	61.5	0.104	0.51246	0.00001	0.51230	−0.7
MB-5	0.16	25,908	0.00002	0.70358	0.00001	0.703578	11.7	57.8	0.122	0.51248	0.00001	0.51230	−0.8
MB-6	0.24	4171	0.00017	0.70366	0.00001	0.703662	10.1	32.4	0.188	0.51248	0.00001	0.51220	−2.7
MB-7	0.09	28,135	0.00001	0.70358	0.00002	0.703582	9.78	42.6	0.138	0.51249	0.00001	0.51228	−1.1
MB-8	0.18	7457	0.00007	0.70384	0.00002	0.703844	10.9	37.1	0.177	0.51257	0.00001	0.51230	−0.8

Sr and Nd initial ratios and epsilon Nd values were calculated based on the 232 Ma age reported by Ying et al. (2017). $^{87}Rb/^{86}Sr$ and $^{147}Sm/^{144}Nd$ values were calculated based on ICP-MS-determined elemental abundances and are associated with relative uncertainties of between 3 and 5% (2σ level).

The initial Pb isotopic values for carbonate grains from the MCC carbonatites define a wide range of values for $^{206}Pb/^{204}Pb$ (17.07–41.21), $^{207}Pb/^{204}Pb$ (15.46–16.90), and $^{208}Pb/^{204}Pb$ (37.67–40.49; Table 5) and are similar to those from Xu et al. (2014). A Pb-Pb secondary isochron yields an age of 594 ± 12 Ma and a lower intercept age of 1469 Ma with the Stacey and Kramers (1975) Pb evolution growth curve. The secondary Pb-Pb isochron date is older than both the Th-Pb dates for zircon of 442.6 ± 4.0 Ma for syenite and 426.5 ± 8.0 Ma for carbonatite from the MCC (Ying et al., 2017) and the Sm-Nd errorchron ages reported here.

5. Discussion

5.1. Overprint and timing of REE hydrothermal mineralization

Carbonatite-hosted REE deposits typically involve both magmatic and late-stage hydrothermal activity, in particular for those associated with significant ore deposits (e.g., Fan et al., 2014; Poletti et al., 2016; Smith et al., 2015). The timing of magmatism vs. hydrothermal activity is variable as it can be essentially simultaneous (e.g., Kizilcaoren fluorite–barite–REE deposit; Gültekin et al., 2003; Nikiforov et al., 2014), or completely unrelated (e.g., Bayan Obo carbonatite complex; Liu et al., 2018).

The occurrence of late-stage metasomatism affecting the MCC has been recently reported as Triassic in age (between 232 and 240 Ma) based on U-Pb dates for monazite and columbite from the MCC carbonatites (Xu et al., 2014; Ying et al., 2017). The chondrite-normalized REE patterns for carbonate investigated here show enrichment in LREEs, which may in part be the result of the late-stage metasomatism (Fig. 4a). Moreover, $\delta^{18}O$ and $\delta^{13}C$ isotope signatures are useful and effective tracers to evaluate possible mantle source(s), contamination or hydrothermal processes (e.g. Deines, 1989; Keller and Hoefs, 1995; Nelson et al., 1988). For example, late-stage metasomatism and hydrothermal activity within the MCC may have produced the heavier $\delta^{18}O$ values recorded for the carbonate separates (Fig. 5). It is well established that elevated $\delta^{18}O$ values in carbonatites may be attributed to low-temperature alteration (e.g., Simonetti et al., 1995), which results in much heavier C and O isotope values ($\delta^{18}O > 14‰$; Denies, 1989). In this study, there are 2 carbonate samples (MB-3A, -3B) that yield $\delta^{18}O$ values that fall within the PIC, whereas the remaining samples are characterized by heavier signatures that range up to +12.51‰ (Fig. 5). The combined $\delta^{18}O$ and $\delta^{11}B$ compostions (Fig. 6) define two trends that seem to converge towards the PIC box. In Fig. 6a, four samples (MB-2, -3B, -4B, 7) define a vertical array with constant $\delta^{11}B$ compositions at ~ − 7‰ and varying $\delta^{18}O$ values that may be attributed

Table 5
Pb isotope data for carbonate separates from the MCC carbonatites.

Sample	U (ppm)	Pb (ppm)	Th (ppm)	$^{238}U/^{204}Pb$	$^{235}U/^{204}Pb$	$^{232}Th/^{204}Pb$	$^{206}Pb/^{204}Pb$	2σ	$^{207}Pb/^{204}Pb$	2σ	$^{208}Pb/^{204}Pb$	2σ
MB-1	4.00	4.58	0.65	67.2	0.48	11.3	33.117	0.0005	16.408	0.0003	38.496	0.0008
MB-2	0.07	2.32	1.83	1.85	0.01	52.3	18.707	0.0007	15.550	0.0007	39.417	0.0021
MB-3A	0.95	2.38	0.15	25.0	0.18	3.96	18.011	0.0004	15.511	0.0003	38.225	0.0009
MB-3B	0.20	2.13	0.05	5.75	0.04	1.60	17.749	0.0004	15.495	0.0004	37.972	0.0012
MB-4A	0.45	11.2	0.52	2.53	0.02	3.06	19.307	0.0004	15.582	0.0004	37.705	0.0010
MB-4B	0.16	6.43	0.20	1.56	0.01	2.03	20.111	0.0004	15.632	0.0003	37.760	0.0010
MB-5	1.23	5.72	0.23	18.2	0.13	3.51	41.891	0.0011	16.935	0.0006	38.282	0.0017
MB-6	1.52	3.16	0.70	32.6	0.23	15.5	20.969	0.0008	15.678	0.0008	40.674	0.0026
MB-7	0.45	3.05	0.39	9.36	0.07	8.35	19.321	0.0007	15.586	0.0007	38.279	0.0023
MB-8	0.53	4.79	0.38	7.21	0.05	5.26	19.724	0.0007	15.605	0.0008	38.544	0.0027

| Sample	$^{207}Pb/^{206}Pb$	2σ	$^{208}Pb/^{206}Pb$	2σ	$^{206}Pb/^{204}Pb$ (i)	$^{207}Pb/^{204}Pb$ (i)	$^{208}Pb/^{204}Pb$ (i)
MB-1	0.49546	0.000004	1.162	0.00001	30.59	16.28	38.36
MB-2	0.83125	0.000012	2.107	0.00006	18.64	15.55	38.80
MB-3A	0.86124	0.000010	2.122	0.00003	17.07	15.46	38.18
MB-3B	0.87300	0.000008	2.139	0.00002	17.53	15.48	37.95
MB-4A	0.80709	0.000006	1.953	0.00002	19.21	15.58	37.67
MB-4B	0.77731	0.000006	1.878	0.00002	20.05	15.63	37.74
MB-5	0.40425	0.000005	0.914	0.00002	41.21	16.90	38.24
MB-6	0.74767	0.000013	1.940	0.00006	19.74	15.62	40.49
MB-7	0.80670	0.000014	1.981	0.00006	18.97	15.57	38.18
MB-8	0.79115	0.000014	1.954	0.00007	19.45	15.59	38.48
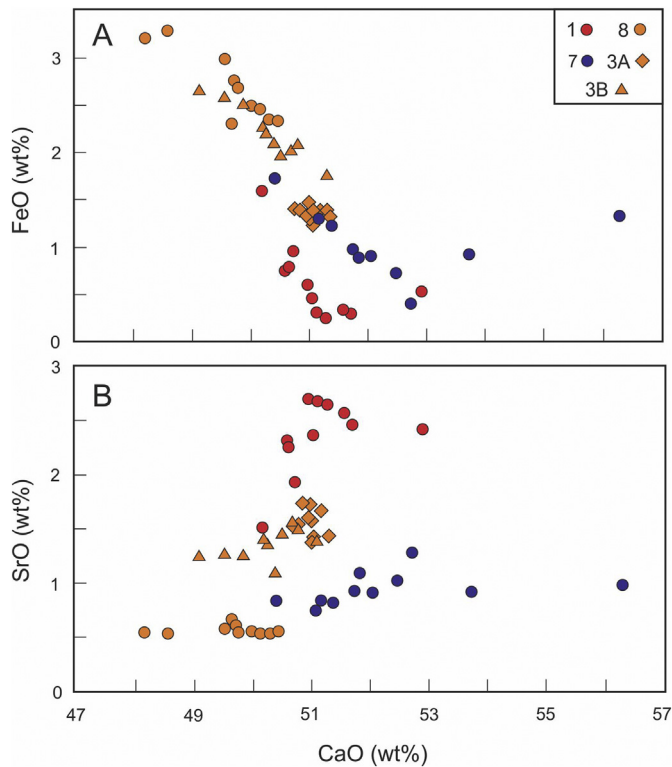
Fig. 3. Diagrams illustrating the major and minor element compositions obtained by electron microprobe analyses for calcites examined from carbonatite samples (MB-1, -3A, -3B, -7, -8) investigated here. (A) FeO (wt%) and (B) SrO (wt%) vs. CaO (wt%).

Fig. 4. (A) Chondrite-normalized rare earth element patterns for carbonate separates from MCC carbonatites investigated here. Grey field in background outlines carbonatite data from Xu et al. (2010). The MCC samples are separated into 3 groups based on their level of LREE enrichment. Chondrite values are from McDonough and Sun (1995). (B) Plot of boron vs LREEs abundances for carbonate separates from MCC carbonatites examined in this study. For this plot and all subsequent diagrams, numbers next to data points refer to sample numbers (listed in Table 1).
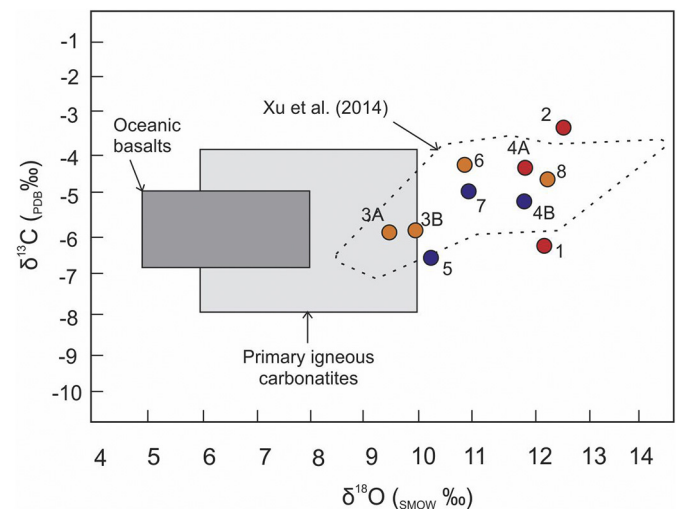
Fig. 5. Carbon and oxygen isotopic compositions for carbonate separates from the MCC carbonatites are plotted in relation to the primary igneous carbonatite box and field for oceanic island basalts (Deines, 1989; Keller and Hoefs, 1995). Dotted field outlines range of C and O isotope values for Miaoya carbonatites reported by Xu et al. (2014).

to closed-system fractional crystallization; their boron isotope compositions are within the range typical of values for melts derived from asthenospheric MORB-like mantle (−7 ± 1‰; Chaussidon and Jambon, 1994). However, melt differentiation involving closed-system fractional crystallization is not corroborated by the major and minor element data reported here (Fig. 3, Table 1), and thus the B and O isotopic variability may indeed be inherited from their mantle source region. The remaining samples define a positive correlation between B and O isotope values, which may be explained by either crustal contamination or late-stage hydrothermal activity (Fig. 6a). In contrast, there is no significant correlation between the $\delta^{13}C$ and $\delta^{11}B$ values since these seem to be randomly scattered to the right of the PIC box (Fig. 6b), and this feature may be consistent with the occurrence of a late-stage hydrothermal event or crustal contamination. This result may be attributed to the buffering capacity of carbonatites in relation to overprinting their carbon isotopic composition during late-stage hydrothermal processes (e.g., Deines, 1989; Xu et al., 2014).

Open-system behavior may also be evaluated using standard two-component mixing diagrams (Fig. 7), which plots the Sr and Nd isotope compositions against the reciprocal values of their respective Sr and Nd abundances. Two component mixing between distinct endmembers typically results in a linear correlation, however, this is clearly not the case for the samples examined here (Fig. 8). The initial $^{87}Sr/^{86}Sr$ compositions are more variable (~0.70357 to ~0.70384) compared to their corresponding initial $^{143}Nd/^{144}Nd$ values, which are essentially within analytical uncertainty relative to one another with the exception of one sample (MB-6; Fig. 7). If late-stage, hydrothermal activity involved a fluid/melt of similar Sr and Nd isotopic compositions to that of the original parental carbonatite magma, then such a
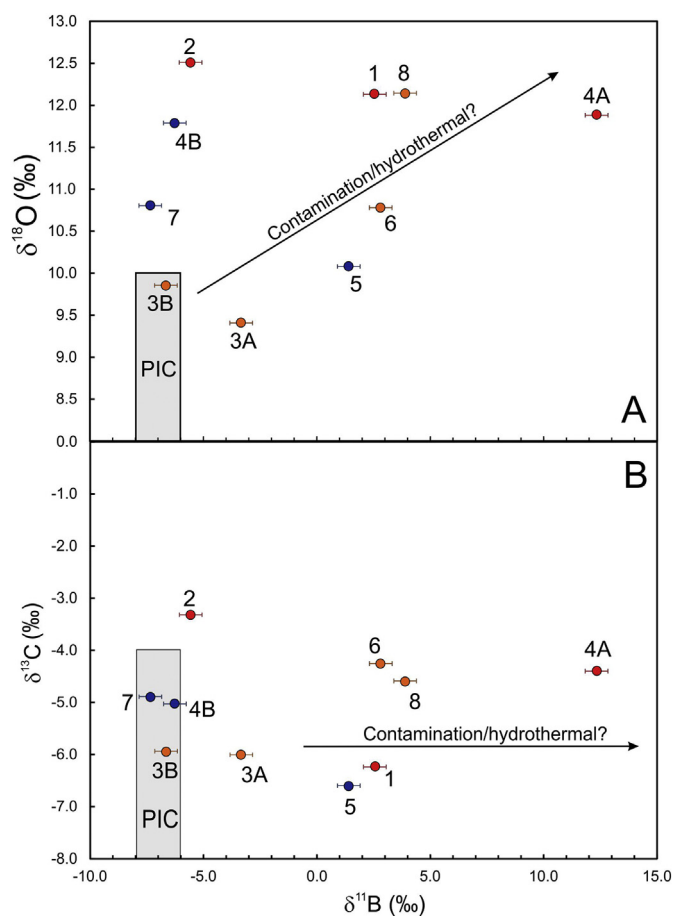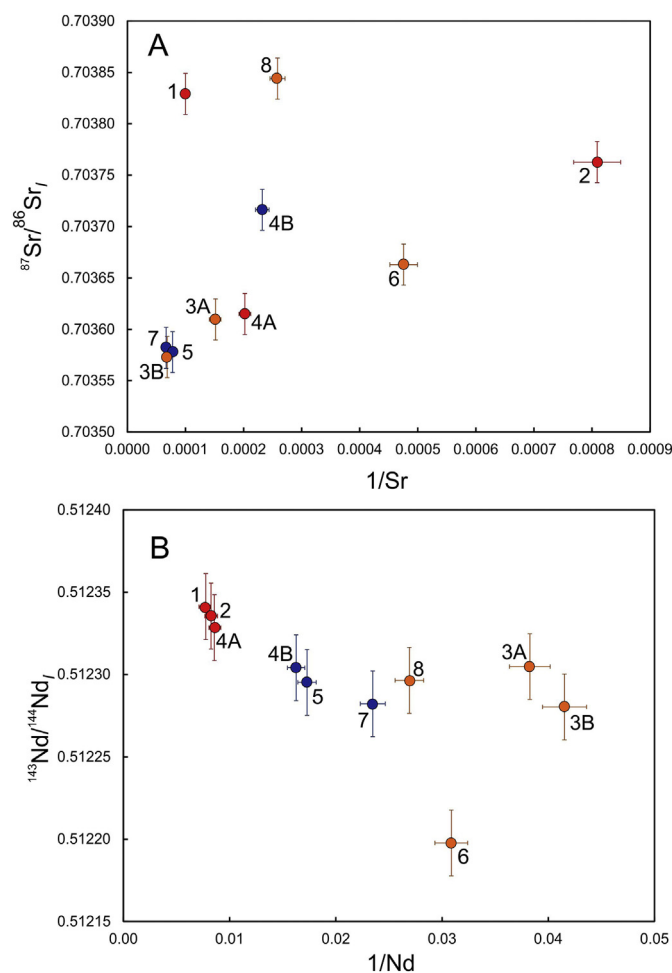
Fig. 6. Plots of δ¹⁸O (A) and δ¹³C (B) vs δ¹¹B isotope signatures for carbonate separates from MCC carbonatites investigated here. PIC = field for Primary Igneous Carbonatites defined after Deines (1989) and Keller and Hoefs (1995) for δ¹³C and δ¹⁸O isotope compositions, and Chaussidon and Jambon (1994) for δ¹¹B isotope signature of typical asthenospheric mantle.
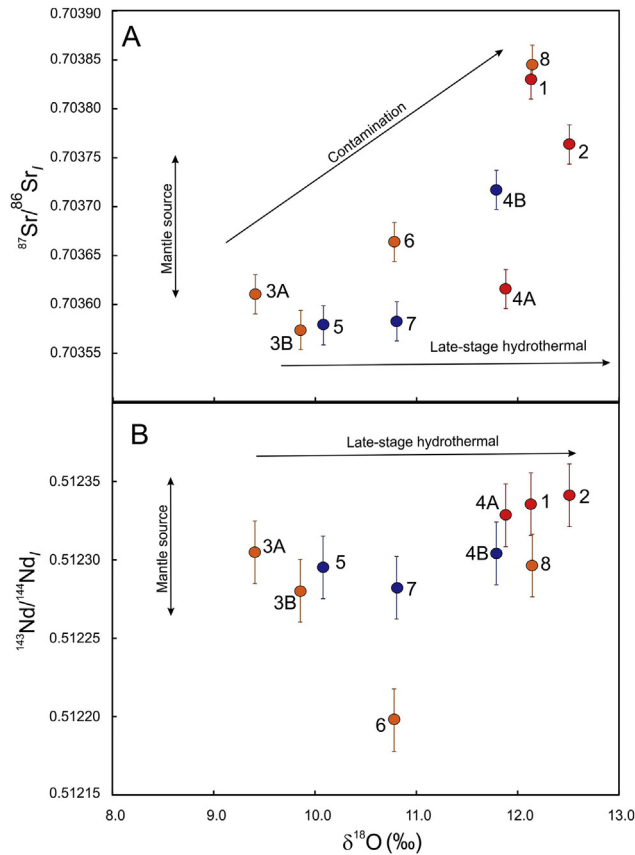

Fig. 7. Plots of initial ⁸⁷Sr/⁸⁶Sr(*I*) vs 1/Sr (A) and initial ¹⁴³Nd/¹⁴⁴Nd(*I*) compositions vs 1/Nd (B) for carbonate separates from the MCC carbonatites.

scenario would result in a horizontal lines in Fig. 7; this is essentially the case for Nd (Fig. 7b) with the exception of one sample, but not for Sr (Fig. 7a). Thus, one possible interpretation is that the late-stage, REE-rich hydrothermal fluid completely overprinted any possible, original Nd isotope heterogeneities within the carbonatites inherited from their mantle source region. It is difficult to determine whether-or-not the variable initial ⁸⁷Sr/⁸⁶Sr ratios preserve mantle source heterogeneities, or reflect open-system behavior, such as crustal contamination. To this end, comparison between initial Sr and Nd isotope ratios and their corresponding δ¹⁸O values (Fig. 8) demonstrates that not all of the results can be attributed to solely a low-temperature, late-stage hydrothermal event. The latter is clearly a more viable interpretation based on the horizontal array defined by the initial Nd vs. O isotope values (Fig. 8b); this feature supports the notion that the late-stage hydrothermal event involved a LREE-rich fluid/melt that completely overprinted both the original Nd and O isotope systematics of the MCC carbonatites.The spread in initial Sr isotope ratios (Fig. 8a) can be attributed to either original mantle source heterogeneity, crustal contamination, and/or late-stage hydrothermal activity, or a mixture of all three processes. Based on the trends shown in Figs. 7 and 8, one possible interpretation is that the Sr abundance of the late-stage fluid/melt was insufficient to completely overprint the precursor Sr isotope signatures of the MCC

carbonatites; this is an analogous interpretation based on the δ¹³C values (Fig. 6b).

In order to better assess the competing hypotheses of mantle source isotopic heterogeneity versus hydrothermal alteration, Fig. 9 compares the abundances of Ba for the carbonate fractions examined here to their corresponding Sr and total REE abundances, and the δ¹¹B and δ¹⁸O_SMOW isotope values. Barium and Sr are two trace elements that are typically abundant within magmatic carbonate, and therefore can be used to monitor fractional crystallization of calcite within carbonatitic melts. For all of the comparative plots shown in Fig. 9, the data are completely scattered and do not exhibit any significant correlations, which indicate that the late-stage hydrothermal activity has not perturbed the Sr and Ba concentrations. Hence, the results shown in Fig. 9 would suggest that the Miaoya carbonates analysed here represent discrete, partial melt fractions (i.e., different generations of carbonate) that are not co-genetically related to one parental magma. This interpretation is supported by the lack of correlations in the major and minor element compositions for the carbonates investigated here (Fig. 3; Table 1). However, the question remains as to whether the elevated REE abundances and δ¹⁸O values for samples MB-1, −2, and -4A are primary (magmatic) signatures, or these are the result of late-stage hydrothermal activity. As pointed out by Broom-Fendley et al. (2017), C and O isotope values in REE-rich carbonate rocks should not be

Fig. 8. Diagrams of initial $^{87}Sr/^{86}Sr(I)$ (A) and initial $^{143}Nd/^{144}Nd(I)$ (B) compositions vs $\delta^{18}O$ values for carbonate separates from the MCC carbonatites.

used to extrapolate fluid sources and temperatures of formation. However, the relative homogeneity of the initial $^{143}Nd/^{144}Nd$ ratios for the samples investigated here (Figs. 7b, 8b) is rather suspect given the variation defined by the Sr and B (and Pb; Table 5) isotope systems (Figs. 7a, 8a, 9d, 11a).

Fig. 10 displays the comparison between the abundances of LREEs and $\delta^{18}O$ and $\delta^{11}B$ compositions for the carbonate samples examined here. It is clear that there is a significant correlation ($R^2 = 0.49$) between $\delta^{18}O$ values and the LREE abundances for samples that contain moderate- to high-levels of LREE enrichment (Fig. 10a), whereas random scatter characterizes the relationship between $\delta^{11}B$ values and LREE (and Ba) contents (Figs. 9, 10b). The positive correlation between O isotope compositions and total LREE abundances for six samples shown in Fig. 10a is consistent with the interpretation that a low-temperature, late-stage, ~232 Ma old hydrothermal event involved a REE-rich fluid/melt. The lack of co-variance between $\delta^{11}B$ values and LREE contents (Fig. 10b) suggests that the late-stage hydrothermal event did not pervasively perturb the B isotope composition of the carbonatite samples investigated here; a finding that is also corroborated by the lack of correlation between B and LREE contents (Fig. 4b). Thus, the B isotope compositions reported here may in fact represent signatures inherited from their mantle source region, and when combined with the other isotope systems, provide meaningful information in relation to carbonatite melt petrogenesis.

The petrogenetic history and time of emplacement of the MCC is somewhat complicated based on the geochronological results from previous investigations (Xu et al., 2014, 2015; Zhu et al., 2017) since reported ages span from 766 to 147 Ma. Isochron age which was calculated using Isoplot (v.3.0) excel-based macro (Ludwig, 2003; not shown) clearly indicates that the Nd

isotope systematics of the carbonate samples investigated here have been perturbed since they define an errorchron age of ~151 Ma; this result corroborates the younger dates of 232 ± 4.5 and ~240 Ma obtained for columbite and monazite from MCC carbonatites, respectively (Ying et al., 2017). The older errorchron date of 794 ± 470 Ma based on literature data (Xu et al., 2014) is consistent with the older age of 426.5 ± 8.0 reported for zircon from carbonatite (Ying et al., 2017). Thus, there are clearly two significant events that have impacted the carbonatites from MCC, which are separated by several hundreds of million of years. The older event at ~430 Ma represents the timing of carbonatite magmatism, whereas the younger age most likely corresponds to the main episode of hydrothermal overprinting and REE mineralization. Of interest, the samples characterized by the lowest $^{147}Sm/^{144}Nd$ ratios (MB-1, −2, and -4A; Table 4) contain the highest LREE contents (Fig. 4b), which is consistent with the preferential increase in Nd over Sm abundances as a result of the REE mineralization.

The Pb isotope ratios for the carbonate samples investigated here yield a secondary Pb-Pb isochron age of 594 ± 12 Ma (calculated using IsoPlot v.3.0; Ludwig, 2003; not shown), which obviously does not represent a meaningful geologic age but most likely represents a mixing line. The secondary isochron intercepts the Stacey and Kramers (1975) Pb isotope growth curve at 1469 Ma, which most likely represents the age of the crustal component (e.g., Paleo-to Neoproterozoic Wudang Complex; Huang, 1993) involved in the two component mixing.

In summary, the results reported here provide additional evidences for the two geological events affecting the MCC. The younger event corresponds to the late-stage metasomatism within the South Qinling, which may be associated with the closure of the Mianlue ocean during the Triassic. The older event is associated with the alkaline and carbonatite magmatism that formed earlier in the Silurian during the opening of the same Mianlue ocean (e.g., Ying et al., 2017).

### 5.2. Mantle sources vs. open-system behavior

Xu et al. (2014) conducted a geochemical and isotopic investigation of the carbonatites and associated syenites from the MCC, and concluded that these two rock types are not petrogenetically related. Moreover, Xu et al. (2014) argue that the MCC carbonatites were derived from a primary carbonate magma generated by direct partial melting of upper mantle. Compared to the Sr, Nd, O, and C isotope results for carbonatites reported in Xu et al. (2014), the ratios for these same isotope systems presented here are similar and overlap those previously published values. However, as with the Pb isotope ratios reported in this study, Xu et al. (2014) also document extremely variable Pb isotopic values that vary between the HIMU and EM1 mantle end-members (Zindler and Hart, 1986). Based on the heavier $\delta^{13}C$ values for the MCC carbonatites, Xu et al. (2014) suggested that these reflect incorporation of recycled inorganic carbon within their mantle source region. In summary, Xu et al. (2014) concluded that the parental carbonatite magma for the MCC was derived from a source incorporating the Mianlue oceanic crust mixed with an asthenospheric (or deeper) mantle; the latter contains a deep-seated, Proterozoic carbonate component recycled via mantle convection or localized upwelling.

Recently, Hulett et al. (2016) adopted, for the first-time, the use of B isotope compositions of carbonatites to monitor the input of recycled carbon of crustal origin within carbonatites located on different continents and of varying age. Mantle-derived boron of crustal origin may be characterized by heavier $\delta^{11}B$ values (discussed in Hulett et al., 2016) compared to that
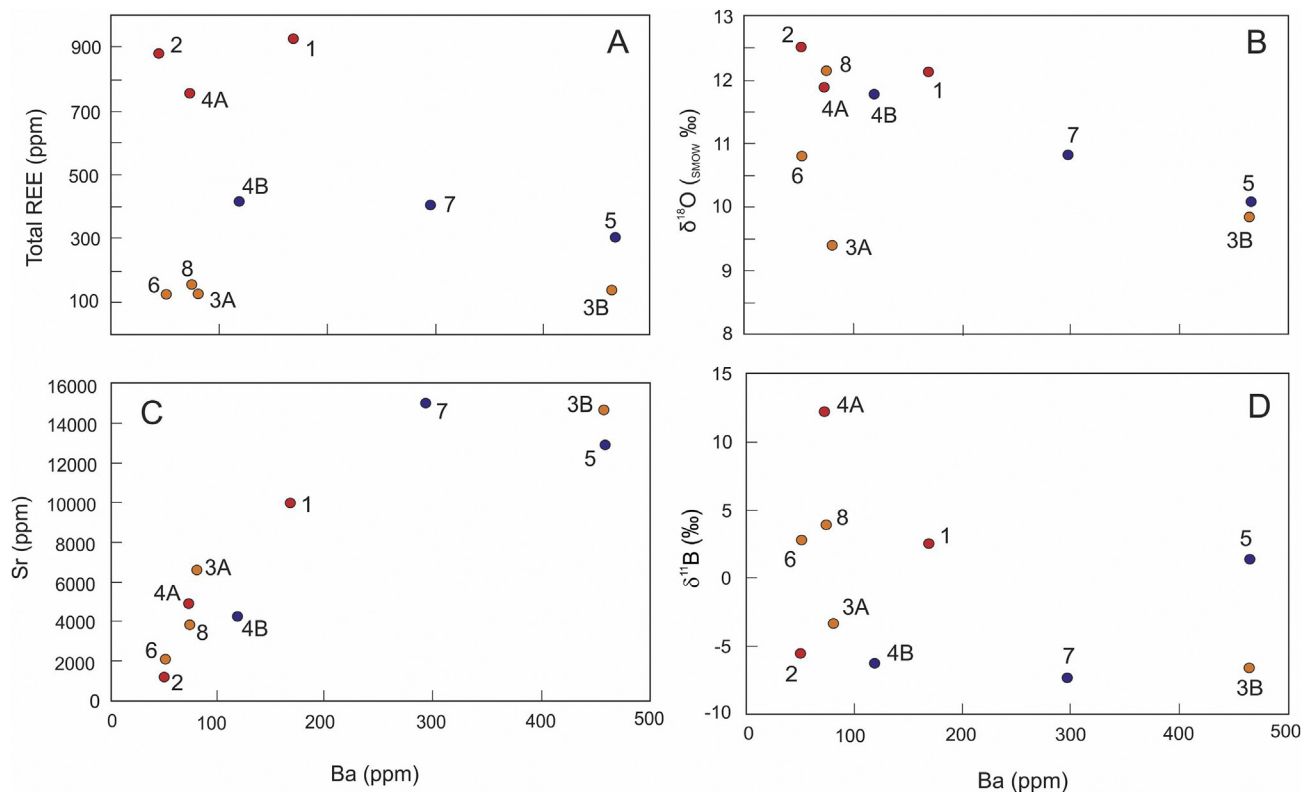
Fig. 9. (A) Plots of total REE abundances (ppm), (B) $\delta^{18}O_{SMOW}$ (‰), (C) Sr (ppm), and (D) $\delta^{11}B$ (‰) vs. Ba (ppm) contents for Miaoya carbonates investigated here.

of typical asthenospheric mantle (-7 ± 1‰; Chaussidon and Jambon, 1994). Based on the chemical and isotopic data illustrated in Figs. 10 and 11, it can be determined which of the samples investigated here retain their isotope signatures inherited from their mantle source. For instance, if it is assumed that samples with either the lowest LREE contents (≤ 150 ppm), lightest $\delta^{18}O$ values and/or asthenospheric-like $\delta^{11}B$ compositions (Fig. 10) have been least affected by the late-stage, low temperature alteration event, then there are a total of 7 samples (MB-3A, -3B, -4B, -6, -7, and -8) that meet these criteria; the B, O, Sr, and Nd isotope compositions for samples MB-1, -2, $-4A$, and -5 have clearly been affected by the late-stage hydrothermal event. In Fig. 11a, samples MB-4A and MB-5 display similar Sr isotope compositions with variable $\delta^{11}B$ values, and this trend is consistent with an interpretation involving late-stage hydrothermal activity. The remaining samples (with the exception of MB-1 and -2), in general, show a positive correlation between their B and Sr isotope signatures, which may be attributed to original mantle source heterogeneity (Fig. 11a). This finding also corroborates the interpretation of Xu et al. (2014) for the presence of recycled crustal C within the carbonatites from the MCC. Of note, sample MB-6 is the sole sample that seems to have retained its original and much lower initial Nd isotope composition (Fig. 11b), which also corroborates the presence of a heterogeneous mantle source that contains recylced crustal material. Based on the 6 carbonate samples that are deemed to be least (if any) affected by the late-stage hydrothermal activity, the $\delta^{11}B$ values exhibit a total range from ~ -7 to $+4$‰; this feature is consistent with the findings of Hulett et al. (2016), which indicate that young carbonatites (<300 million years in age) preferentially record heavier boron isotope compositions attributed to sampling of recycled crustal material (Fig. 12). The corresponding initial Sr and Nd isotope data for
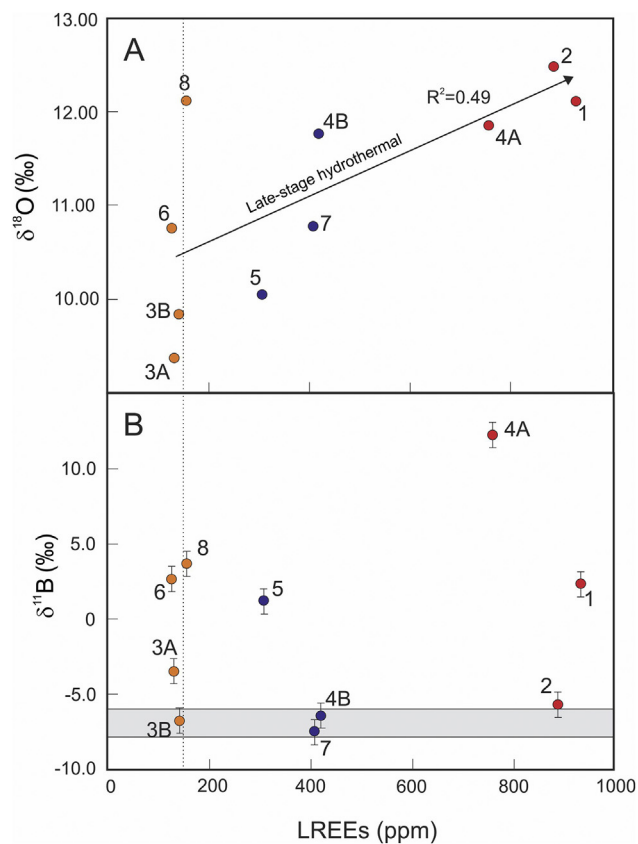
Fig. 10. Diagrams of $\delta^{18}O$ (A) and $\delta^{11}B$ values (B) vs LREE abundances for carbonate separates from the MCC carbonatites. Grey field = range of $\delta^{11}B$ isotope values for typical asthenospheric mantle (Chaussidon and Jambon, 1994).
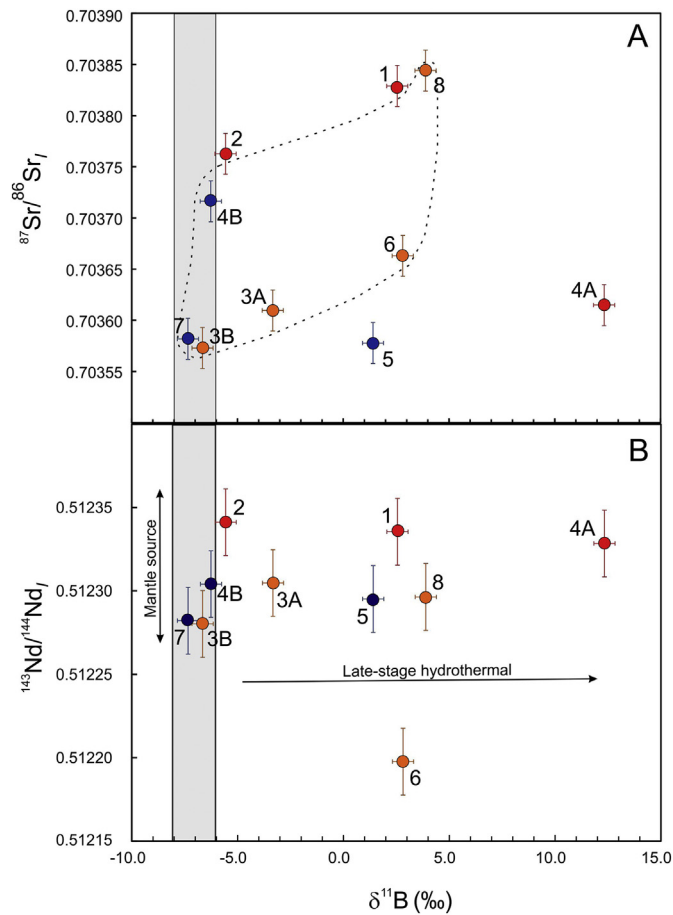
Fig. 11. Diagrams of initial $^{87}Sr/^{86}Sr(I)$ (A) and initial $^{143}Nd/^{144}Nd(I)$ (B) compositions vs $\delta^{11}B$ values for carbonate separates from the MCC carbonatites. Dotted line in (A) outlines field that represents the B and Sr isotopic heterogeneity that characterizes the mantle source region for the MCC carbonatites. Grey field = $\delta^{11}B$ isotope values for asthenospheric mantle (-7 ± 1‰; Chaussidon and Jambon, 1994).
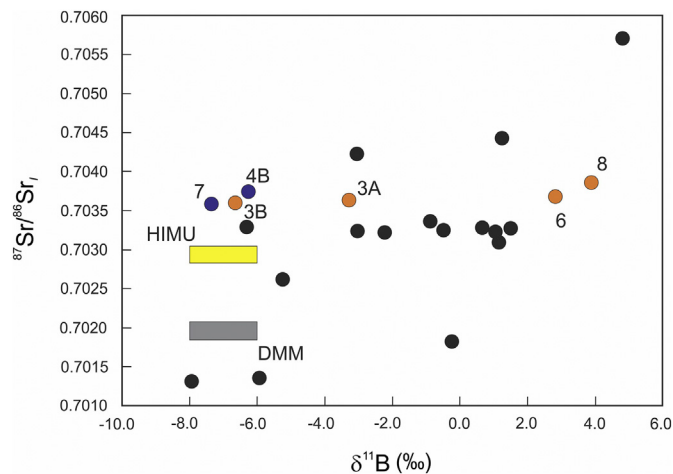
Fig. 12. Plot of initial $^{87}Sr/^{86}Sr(I)$ ratios isotope values against versus their respective $\delta^{11}B$ values for Miaoya carbonatite samples investigated here (colored circles with sample numbers). These are compared to those for carbonatite occurrences worldwide (black circles) from Hulett et al. (2016). Initial Sr isotope values for HIMU (yellow box) and DMM (grey box) values are from Zindler and Hart (1986); asthenospheric $\delta^{11}B$ values of -7 ± 1‰ (Chaussidon and Jambon, 1994) are attributed to both of these two mantle components. In general, the higher Sr and B isotope values for carbonatites compared to those for DMM and HIMU are consistent with the presence of recycled crustal carbon within their mantle source region (after Hulett et al., 2016), (For interpretation of the references to colour in this figure legend, the reader is referred to the web version of this article.)

these same seven samples are consistent with derivation from a mixed HIMU-EMI mantle source, a finding argued by Xu et al. (2014) and with the isotope compositions of young carbonatites worldwide (e.g., Bell and Simonetti, 2010).

In summary, the combined geochemical and isotope results reported in this study clearly demonstrate the utility and effectiveness in investigating the boron isotopic composition of carbonatites. When combined with geochemical data (Figs. 9 and 10) and the remaining isotope systems (Fig. 6), $\delta^{11}B$ values are critical in assessing and confirming the extent of hydrothermal alteration of the MCC carbonate samples examined here. Consequently, this allowed for a more accurate interpretation of the isotopic data in relation to the characteristics of their mantle source, in particular for the Sr isotope systematics. Ultimately, the results presented here corroborate previous interpretations advocating the involvement of recycled crustal carbon within the MCC carbonatites (Xu et al., 2014). Moreover, it is clear that the Nd and Pb isotope systems of the MCC carbonatites have been severely perturbed by the late-stage, low-temperature hydrothermal activity involving REE-rich fluid/melt, and these should be used with caution in relation to evaluating mantle source region characteristics.

6. Conclusions

The B isotope signatures reported here, a first for the Miaoya carbonatite complex, when combined with radiogenic (Sr, Nd, and Pb) and stable (O and C) isotope results provide more detailed information about its petrogenetic evolution and deciphering the chemical nature of the mantle source.

On the basis of the geochemical and Sm-Nd isotope data documented in this study, it is clear that the petrogenetic history of the MCC involved two major geological events. The first represents carbonatite melt formation and emplacement at ~440 million years ago, and this was followed by a significant low-temperture, hydrothermal event that involved a REE-rich fluid/melt. The former is interpreted to represent melting associated with an extensional environment during the Silurian, whereas the latter is associated closure of the Mianlue Ocean during the Triassic period. The late-stage hydrothermal event overprinted the Nd and Pb isotope compositions for most of the carbonatite samples examined here, whereas a majority of the samples preserve their variable B and Sr isotope values inherited from their mantle source. The latter combined indicate carbonatite melt generation from a heterogenous mantle that incorporated recycled crustal material. This result is consistent with the B and Sr isotope systematics previously reported for young (<300 Ma old) carbonatites worldwide.

Appendix A. Supplementary data

Supplementary data to this article can be found online at https://doi.org/10.1016/j.lithos.2018.10.018.

References

Bailey, D.K., 1993a. Carbonate magmas. J. Geol. Soc. Lond. 150, 637–651.

Bailey, D.K., 1993b. Petrogenetic implications of the timing of alkaline, carbonatite, and kimberlite igneous activity in Africa. S. Afr. J. Geol. 96, 67–74.

Bell, K., Simonetti, A., 1996. Carbonatite magmatism and plume activity: implications from the Nd, Pb and Sr isotope systematics of Oldoinyo Lengai. J. Petrol. 37, 1321–1339.

Bell, K., Simonetti, A., 2010. Source of parental melts to carbonatites–critical isotopic constraints. Mineral. Petrol. 98, 77–89.

Bell, K., Tilton, G.R., 2001. Nd, Pb and Sr Isotopic Compositions of East African Carbonatites: evidence for Mantle Mixing and Plume Inhomogeneity. J. Petrol. 42, 1927–1945.

Bonadiman, C., Coltorti, M., Duggen, S., Paludetti, L., Siena, F., Thirwall, M.F., Upton, B.G.J., 2008. Palaeozoic subduction-related and kimberlite or carbonatite metasomatism in the Scottish lithospheric mantle. Geol. Soc. Lond. Spec. Publ. 293, 303–333.

Broom-Fendley, S., Wall, F., Spiro, B., Ullmann, C.V., 2017. Deducing the source and composition of rare earth mineralising fluids in carbonatites: insights from isotopic (C, O,^{87}Sr/^{86}Sr) data from Kangankunde, Malawi. Contrib. Mineral. Petrol. 172, 96–113.

Chaussidon, M., Jambon, A., 1994. Boron content and isotopic composition of oceanic basalts: geochemical and cosmochemical implications. Earth Planet. Sci. Lett. 259, 541–556.

Chen, W., Lu, J., Jiang, S.Y., Ying, Y.C., Liu, Y.S., 2018. Radiogenic Pb reservoir contributes to the rare earth element (REE) enrichment in South Qinling carbonatites. Chem. Geol. 494, 80–95.

Cooper, A.F., Boztuğ, D., Palin, M.J., Martin, C.E., Numata, M., 2011. Petrology and petrogenesis of carbonatitic rocks in syenites from Central Anatolia, Turkey. Contrib. Mineral. Petrol. 161, 811–828.

Dasgupta, R., Walker, D., 2008. Carbon solubility in core melts in a shallow magma ocean environment and distribution of carbon between the Earth's core and the mantle. Geochim. Cosmochim. Acta 72, 4627–4641.

Deines., P., 1989. Stable isotope variations in carbonatites. In: Bell, K. (Ed.)Carbonatites: Genesis and Evolution. Unwin-Hyman, London, pp. 301–359.

Deng, L.L., Liu, Y., Gao, S., 2014. Pacific Slab Subduction-induced Carbonatite Mantle Metasomatism in the Eastern North China Craton. American Geophysical Union, Fall Meeting, abstract #V13B-4774.

D'Orazio, M., Innocenti, F., Tonarini, S., Doglioni, C., 2007. Carbonatites in a subduction system: the Pleistocene alvikites from Mt. Vulture (southern Italy). Lithos 98, 313–334.

Fan, H.R., Hu, F.F., Yang, K.H., Pirajno, F., Liu, X., Wang, K.Y., 2014. Integrated U–Pb and Sm–Nd geochronology for a REE-rich carbonatite dyke at the giant Bayan Obo REE deposit, Northern China. Ore Geol. Rev. 63, 510–516.

Fischer, T.P., Burnard, P., Marty, B., Hilton, D.R., Füri, E., Palhol, F., Sharp, Z.D., Mangasini, F., 2009. Upper-mantle volatile chemistry at Oldoinyo Lengai volcano and the origin of carbonatites. Nature 459, 77–80.

Gittins, J., Harmer, R.E., 2003. Myth and reality in the carbonatite–silicate rock association. Period. Mineral. 72, 19–26.

Gültekin, A.H., Örgün, Y., Suner, F., 2003. Geology, mineralogy and fluid inclusion data of the Kizilcaoren fluorite- barite- REE deposit, Eskisehir, Turkey. J. Asian Earth Sci. 21, 365–376.

Hou, Z.Q., Tian, S., Yuan, Z., Xie, Y., Yin, S., Yi, L., Fei, H., Yang, Z., 2006. The Himalayan collision zone carbonatites in western Sichuan, SW China: Petrogenesis, mantle source and tectonic implication. Earth Planet. Sci. Lett. 244, 234–250.

Hou, Z., Liu, Y., Tian, S., Yang, Z., Xie, Y., 2015. Formation of carbonatite-related giant rare-earth-element deposits by the recycling of marine sediments. Sci. Rep. 5 (10231), 1–10.

Huang, W., 1993. Huang Multiphase deformation and displacement within a basement complex on a continental margin: the Wudang Complex in the Qinling Orogen, China. Tectonophysics 224 (4), 302–326.

Hulett, S.R.W., Simonetti, A., Rasbury, E.T., Hemming, N.G., 2016. Recycling of subducted crustal components into carbonatite melts revealed by boron isotopes. Nat. Geosci. 9, 904–908.

Jones, A.P., Genge, M., Carmody, L., 2013. Carbonate melts and carbonatites. Rev. Mineral. Geochem. 75, 289–322.

Keller, J., Hoefs, J., 1995. Stable Isotope Characteristics of Recent Natrocarbonatites from Oldoinyo Lengai. Carbonatite Volcanism. IAVCEI Proceedings in Volcanology. Vol. 4, pp. 113–123.

Larsen, L.M., Rex, D.C., 1992. A review of the 2500 Ma span of alkaline-ultramafic, potassic and carbonatitic magmatism in West Greenland. Lithos 28, 367–402.

Lee, W.J., Wyllie, P.J., 1998. Processes of crustal carbonatite formation by liquid immiscibility and differentiation, elucidated by model systems. J. Petrol. 39, 2005–2013.

Lee, W.J., Fanelli, M.F., Cava, N., Wyllie, P.J., 2000. Calciocarbonatite and magnesiocarbonatite rocks and magmas represented in the system CaO-MgO-CO2-H2O at 0.2 GPa. Mineral. Petrol. 68, 225–256.

Ling, W.L., Ren, B.F., Duan, R.C., Liu, X.M., Mao, X.W., Peng, L.H., Liu, Z.X., Cheng, J.P., Yang, H.M., 2008. Timing of the Wudangshan, Yaolinghe volcanic sequences and mafic sills in South Qinling: U-Pb zircon geochronology and tectonic implication. Chin. Sci. Bull. 53, 2192–2199.

Liu, Y.G., Ling, M.X., Williams, I.S., Yang, X.Y., Wang, C.Y., Sun, W., 2018. The formation of the giant Bayan Obo REE-Nb-Fe deposit, North China, Mesoproterozoic carbonatite and overprinted Paleozoic dolomitization. Ore Geol. Rev. 92, 73–83.

Ludwig, K.R., 2003. User's Manual for Isoplot 3.00: A Geochronological Toolkit for Microsoft Excel. Berkeley Geochronology Center, Berkeley, CA, USA.

Luth, R.W., 1993. Diamonds, eclogites, and the oxidation-state of the Earth's mantle. Science 261, 66–68.

McDonough, W.F., Sun, S.S., 1995. The composition of the Earth. Chem. Geol. 120, 223–253.

Mitchell, R.H., 2005. Carbonatites and carbonatites and carbonatites. Can. Mineral. 43, 2049–2068.

Nelson, D.R., Chivas, A.R., Chappell, B.W., McCulloch, M.T., 1988. Geochemical and isotopic systematics in carbonatites and implications for the evolution of ocean-island sources. Geochim. Cosmochim. Acta 52, 1–17.

Nikiforov, A.V., Öztürk, H., Altuncu, S., Lebedev, V.A., 2014. Kizilcaören Ore-bearing Complex with Carbonatites (Northwestern Anatolia, Turkey): Formation Time and Mineralogy of Rocks. Geol. Ore Dep. 56, 35–60.

Poletti, J.E., Cottle, J.M., Hagen-Peter, G.A., Lackey, J.S., 2016. Petrochronological constraints on the origin of Mountain Pass ultrapotassic and carbonatite intrusive suite, California. J. Petrol. 57, 1555–1598.

Russell, J.K., Porritt, L.A., Lavallée, Y., Dingwell, D.B., 2012. Kimberlite ascent by assimilation-fuelled buoyancy. Nature 481, 352–357.

Simonetti, A., Bell, K., Viladkar, S.G., 1995. Isotopic data from the Amba Dongar Carbonatite Complex, west-central India: evidence for an enriched mantle source. Chem. Geol. 122, 185–198.

Simonetti, A., Goldstein, S.L., Schmidberger, S.S., Viladgar, S.G., 1998. Geochemical and Nd, Pb, and Sr isotope data from deccan alkaline complexes-inferences for mantle sources and plume–lithosphere interaction. J. Petrol. 11-12, 1847–1864.

Smith, M.P., Campbell, L.S., Kynicky, J., 2015. A review of the genesis of the world class Bayan Obo Fe-REE-Nb deposits, Inner Mongolia, China: Multistage processes and outstanding questions. Ore Geol. Rev. 64, 459–476.

Spivack, A.J., Edmond, J.M., 1987. Boron isotope exchange between seawater and the oceanic crust. Geochim. Cosmochim. Acta 51, 1033–1043.

Stacey, J.S., Kramers, J.D., 1975. Approximation of Terrestrial Lead Isotope Evolution by a 2-Stage Model. Earth Planet. Sci. Lett. 26, 207–221.

Tappe, S., Foley, S.F., Jenner, G.A., Kjarsgaard, B.A., 2005. Integrating Ultramafic Lamprophyres into the IUGS Classification of Igneous Rocks: Rationale and Implications. J. Petrol. 46, 1893–1900.

Treiman, A.H., Schedl, A., 1983. Properties of carbonatite magma and processes in carbonatite magma chambers. J. Geol. 91, 437–447.

Veksler, I.V., Petibon, C., Jenner, G.A., Dorfman, A.M., Dingwell, D.B., 1998. Trace element partitioning in immiscible silicate–carbonate liquid systems: an initial experimental study using a centrifuge autoclave. J. Petrol. 39, 2095–2104.

Woolley, A.R., 1989. The Spatial and Temporal Distribution of Carbonatites: Carbonatites: Genesis and Evolution. Unwin Hyman. pp. 15–37.

Woolley, A.R., Kjarsgaard, B.A., 2008. Carbonatite occurrences of the world: Map and database. Geological Survey of Canada. Open File Rep. 5796.

Wunder, B., Meixner, A., Romer, R.L., Wirth, R., Heinrich, W., 2005. The geochemical cycle of boron: constraints from boron isotope partitioning experiments between mica and fluid. Lithos 84, 206–216.

Xu, C., Campbell, I.H., Allen, C.M., Chen, Y., Huang, Z., Qi, L., Zhang, G., Yan, Z., 2008. U–Pb zircon age, geochemical and isotopic characteristics of carbonatite and syenite complexes from the Shaxiongdong, China. Lithos 105, 118–128.

Xu, C., Kynicky, J., Chakmouradian, A.R., Campbell, I.H., Allen, C.M., 2010. Trace element modeling of the magmatic evolution of rare earth-rich carbonatite from the Miaoya deposit, Central China. Lithos 118, 145–155.

Xu, C., Chakhmouradian, A.R., Taylor, R.N., Kynicky, J., Li, W., Song, W., Fletcher, I.R., 2014. Origin of carbonatites in the South Qinling orogen: Implications for crustal recycling and timing of collision between the South and North China Blocks. Geochim. Cosmochim. Acta 143, 189–206.

Xu, C., Kynicky, J., Chakmouradian, A.R., Li, X., Song, W., 2015. A case example of the importance of multi-analytical approach in deciphering carbonatite petrogenesis in South Qinling orogen: Miaoya rare-metal deposit, Central China. Lithos 227, 107–121.

Ying, Y., Chen, W., Lu, J., Jiang, S.Y., Yang, Y., 2017. In situ U–Th–Pb ages of the Miaoya carbonatite complex in the South Qinling orogenic belt, Central China. Lithos 290-291, 159–171.

Zhu, J., Wang, L., Peng, S., Peng, L., Wu, C., Qiu, X., 2017. U–Pb zircon age, geochemical and isotopic characteristics of the Miaoya syenite and carbonatite complex, central China. Geol. J. 52, 938–954.

Zindler, A., Hart, S.R., 1986. Chemical dynamics. Annu. Rev. Earth Planet. Sci. 14, 493–571.